Duparchy *et al. Energy Mater.* **2025**, *5*, 500134
DOI: 10.20517/energymater.2025.51

Energy Materials

Article

Open Access

Check for updates

Poorer is better: towards robust, high performance $Mg_2(Si,Sn)$ thermoelectric material by avoiding excess Mg

Amandine Duparchy[1,*], Harshita Naithani[1], Sanyukta Ghosh[1], Michael Parzer[2], Fabian Garmroudi[2], Eckhard Müller[1,3], Johannes de Boor[1,4,*]

[1]Institute for Frontier Materials on Earth and in Space, German Aerospace Center (DLR), Cologne 51147, Germany.
[2]Institute of Solid-State Physics, TU Wien, Vienna 1040, Austria
[3]Institute of Inorganic and Analytical Chemistry, Justus Liebig University Giessen, Giessen 35392, Germany.
[4]Institute of Technology for Nanostructures (NST) and CENIDE, University of Duisburg-Essen, Faculty of Engineering, Duisburg 47057, Germany.

[*]**Correspondence to:** Amandine Duparchy and Prof. Johannes de Boor, Institute of Materials Research, German Aerospace Center (DLR), Linder Höhe, Cologne 51147, Germany. E-mail: amandine.duparchy@dlr.de; Johannes.deBoor@dlr.de

How to cite this article: Duparchy, A.; Naithani, H.; Ghosh, S.; Parzer, M.; Garmroudi, F.; Müller, E.; de Boor, J. Poorer is better: towards robust, high performance $Mg_2(Si,Sn)$ thermoelectric material by avoiding excess Mg. *Energy Mater.* **2025**, *5*, 500134. https://dx.doi.org/10.20517/energymater.2025.51

Received: 28 Feb 2025 **First Decision:** 30 Apr 2025 **Revised:** 7 May 2025 **Accepted:** 16 May 2025 **Published:** 9 Jul 2025

Academic Editor: Yizhong Huang **Copy Editor:** Ping Zhang **Production Editor:** Ping Zhang

Abstract

$Mg_2(Si,Sn)$-based semiconductors constitute promising thermoelectrics (TE), in particular as n-type materials. These are usually synthesized under Mg-excess to compensate for losses of Mg during synthesis and achieve the high carrier concentration required for optimal performance. However, this usage of excess Mg leads to loosely bound Mg in the material which is easily lost during operation, leading to a fast and massive degradation of the TE performance. In this work, we introduce Mg-poor n-type $Mg_2(Si,Sn)$, avoiding excess and loosely bound Mg. We find that (i) employing relatively large nominal Mg deficiency leads nevertheless to single-phase, Mg-poor $Mg_2(Si,Sn)$ by a self-adjustment of the composition during sintering, and (ii) that despite showing a lower dopant efficiency, Sb can be employed to achieve the required optimum carrier concentration, resulting in a figure of merit of $zT = 1.2 \pm 0.2$ at 700 K, comparable to Mg-rich samples. This is confirmed by a comparison of Mg-rich and Mg-poor samples in a single parabolic band model which reveals similar microscopic material parameters such as weighted mobility and scattering constants. Finally, we compare Mg-poor synthesized samples with initially Mg-rich ones that experienced Mg loss. Despite similar global compositions we identify grain boundary scattering to be more pronounced in Mg-depleted samples, marking one of the fundamental reasons for the performance degradation of synthesized Mg-rich synthesized samples. Overall, this work highlights the importance of grain

boundaries on grain boundaries for the performance of TE materials and the successful application of thermodynamic degrees of freedom to address fundamental challenges in TE material systems while retaining promising TE performance.

Keywords: $Mg_2Si_{1-x}Sn_x$, thermoelectric transport properties, single parabolic band model, Mg-related defects, material stoichiometry

INTRODUCTION

As the global energy crisis escalates, the need for sustainable and efficient energy sources is becoming increasingly important[1,2]. Current methods of power generation, such as coal and gas combustion, contribute significantly to environmental degradation and resource depletion. By converting (waste) heat into usable electrical energy, thermoelectric technology offers a promising solution to ease energy demand while reducing our carbon footprint[3]. Thermoelectric (TE) generators are competitive solutions due to their high reliability, absence of mechanical components, extended operation lifespan and low maintenance demands. They have been used mainly in the aerospace field for space probes such as Voyager 1 and 2 (after decades of operation) or in Mars missions with Perseverance and Curiosity rovers[4-6].

The efficiency of TE devices depends on the properties of the employed TE material, evaluated by the thermoelectric figure of merit $zT = \frac{S^2\sigma}{\kappa}T$ at an absolute temperature T. Here, S represents the Seebeck coefficient, σ the electrical conductivity and κ the thermal conductivity[7]. Maximizing the figure of merit is essential for the development of thermoelectric technologies, as it indicates the material's ability to efficiently convert heat into electricity[8,9] at a given temperature gradient. However, the value of zT is limited by the interdependence of the three essential transport properties: S, σ and κ, where κ should be low and the TE power factor $PF = S^2\sigma$ should be high. The Seebeck coefficient and electrical conductivity are largely governed by the charge carrier concentration (n) and the charge carrier mobility (μ). The charge carrier concentration depends on the defect types and concentrations of the semiconducting base material and can be adjusted by doping the material[7]. Generally, TE materials achieve maximum zT for relatively high carrier concentrations (10^{19}-10^{20} cm^{-3}) and the addition of a well-chosen foreign atom will modify the Fermi level, resulting in higher carrier concentration[7].

So far, significant advancements have been made in developing TE materials suitable for intermediate temperatures ranging from 500 K to 900 K, resulting in high figures of merit up to $zT > 2$. Noteworthy examples include PbTe[10], Skutterudites[11], half-Heusler compounds[12] and Mg-based materials such as MgAgSb[13,14], Mg_3Sb_2[15,16] or $Mg_2Si_{1-x}Sn_x$ solid solutions[17,18]. The latter meet several criteria for large scale applicability, including the utilization of lightweight and abundant raw elements (Mg, Si and Sn), low cost, environmental compatibility and excellent thermoelectric performance[19,20]. N-type $Mg_2Si_{1-x}Sn_x$ solid solutions doped with antimony have been optimized showing excellent TE properties ($zT_{max} \sim 1.4$) arising from a degeneracy of the conduction bands (CB) for the composition range x = 0.6 to 0.7 and reduced lattice thermal conductivity due to alloying[18,21,22]. The application potential has been demonstrated by the successful fabrication of prototypes by Kaibe *et al.*[23] using a two-stage BiTe-silicide module, followed by the development of the first full Mg_2(Si,Sn) (used as both p- and n-type) device by Camut *et al.*[24] which achieved conversion efficiencies of 12% with T_h = 550 °C and T_c = 30 °C and 3.6% with T_h = 400 °C and T_c = 25 °C, respectively. Later on, Wieder *et al.*[25] developed a module combining p-type MgAgSb and n-type Mg_2(Si,Sn) leading to an improved efficiency of 6.4%.

Although $Mg_2(Si,Sn)$-based materials feature attractive TE properties and technological advances have been made, its stability remains a major drawback for thermoelectric devices which need to operate at high temperatures. Skomedal *et al.*[26] studied the material stability at high temperature in air, showing the high sensitivity of the material to oxidation. A further well-known challenge is that the Mg stoichiometry in the $Mg_2(Si,Sn)$ solid solutions is difficult to control[27]. Mg content can decrease compared to the target stoichiometry as Mg has a lower melting point and a higher vapor pressure than the other elements involved and thus evaporates easily. This impacts the intrinsic Mg point defect densities and thereby the charge carrier concentration and the functional properties of the material[28,29]. The use of excess Mg in the synthesis process (nominal starting composition $Mg_{2+\delta}(Si,Sn)$) is usually chosen as a strategy to counteract the change in functional properties[30-33]. However, Sankhla *et al.*[34] studied the effect of heat treatment on the stability of material synthesized with excess Mg and demonstrated that changes in transport properties (decrease in carrier concentration) are linked to Mg loss. Recently, Duparchy *et al.*[27] investigated room temperature stability in air of n- and p-type $Mg_2(Si,Sn)$ solid solutions, demonstrating that the p-type material which had been synthesized without Mg excess is stable over time while the n-type degrades. This was traced back to the diffusion of loosely bound Mg in Sn-rich phases via Mg vacancies, leading to subsequent Mg oxidation at the surface and causing gradual changes in the integral material properties. Ghosh *et al.*[35] showed that the dominant Mg diffusion path is through grain boundaries and Sankhla *et al.*[36] developed a microscopic understanding for Mg loss and determined degradation kinetics.

From these experimental results and first-principles calculations on defect densities[37,38], it is clear that $Mg_2(Si,Sn)$ exhibits a finite solubility range with respect to Mg, with compositions between $Mg_{2(1+\delta_1)}(Si,Sn)$ and $Mg_{2(1+\delta_2)}(Si,Sn)$ ($\delta_1 < \delta_2$) being in principle feasible. Here, $Mg_{2(1+\delta_1)}(Si,Sn)$ and $Mg_{2(1+\delta_2)}(Si,Sn)$ represent Mg-poor and Mg-rich thermodynamic states, which represent the lower and upper solubility limit, respectively, and differ by the concentration of intrinsic point defects. This finite width of presumable line phase is typical for TE materials and is, e.g., observed for BiTe and Mg_3Sb_2[39-42], with phase widths δ_2-$\delta_1 < 0.001$. The intrinsic defects with the lowest defect formation energies in $Mg_2(Si,Sn)$ are Mg-related: Mg interstitials (I_{Mg}^{2+}) and Mg vacancies (V_{Mg}^{2-})[38]. Mg interstitials (Mg on the interstitial position) will be the dominant defect under Mg-rich conditions, contributing electrons[27,38]. In Mg-poor samples, Mg vacancies will become more abundant, potentially with defect densities larger than Mg interstitials, acting as acceptor defects, compensating electrons. Hence, it is important to differentiate between: (i) excess Mg which refers to an non-soluble content of elemental Mg in the material, (ii) loosely bound Mg which is part of the crystal lattice but can be removed from it by changing the concentration of point defects and (iii) tightly bound Mg which refers to Mg that is bound in the crystal lattice of Mg-depleted $Mg_2(Si,Sn)$ material and cannot be removed from it without initiating decomposition of the compound into its elemental constituents. Tightly bound Mg is very stable, while Sankhla *et al.*[36] proved that loosely bound Mg is lost before the material starts to decompose and thus the fastest and most important material degradation mechanism. Hence, long-term stability requires the suppression of this loosely bound Mg from the material.

This might in principle be done by impeding Mg diffusion[43], avoiding Mg loss by the use of coatings[44], or potentially most easily by eliminating the loose Mg source. Duparchy *et al.*[27] also demonstrated that p-type materials, which are synthesized without excess Mg and presumably Mg-poor after synthesis[45,46], remain stable over years.

This study aims to overcome the fundamental origin of the instability of n-type Mg_2X by the synthesis of Mg-poor samples. We report for the first time, thermoelectric properties and microstructural analysis of optimized n-type Mg-poor $Mg_{2-\delta}Si_{0.3}Sn_{0.7}$ solid solutions. We find that - compared to the usually employed Mg-rich material - larger amounts of Sb dopant are required to increase the carrier concentration in

$Mg_{2-\delta}Si_{0.3-y}Sn_{0.7}Sb_y$-based solid solutions. This decreased dopant efficiency is expected due to the lower density of Mg interstitials and the formation of compensating defects[47,48] originating from reduced amount of Mg in the nominal composition, but we demonstrate here that the carrier concentration required for optimal thermoelectric performance can be obtained. We furthermore show that the synthesized Mg-poor material undergoes a "self-adjusting" single-phase synthesis, insensitive to the nominal starting composition, leading to highly reproducible TE properties. Such phenomenon is explained by a loss of Mg-Sn melt during the pressure-assisted sintering, driving the material to the well-defined Mg-poor state by a slight adjustment of the Mg and Sn content of the samples.

Microstructural analysis of the samples shows a phase constitution comparable to that of Mg-rich samples and high temperature property measurements confirm that it is possible to synthesize a highly doped Mg-poor solid-solution, with good and reproducible TE properties, comparable to those of Mg-rich solid-solutions. Furthermore, extracting the microscopic material parameters, such as the effective mass and scattering constants, using a single-parabolic band analysis reveals similar results for Mg-poor and Mg-rich samples. However, comparing the synthesized Mg-poor material with synthesized Mg-rich samples that are fully Mg-depleted due to annealing shows a drastic performance reduction of the synthesized Mg-rich samples and detrimental grain boundary scattering, while the synthesized Mg-poor samples show only very limited grain boundary scattering. Besides being a possible solution towards improved material stability, Mg-poor material leads to better reproducibility as there is less chance for Mg loss during synthesis.

EXPERIMENTAL

Material synthesis

N-type $Mg_{2-\delta}Si_{1-x-y}Sn_xSb_y$ (δ = 0.1, 0.05; x = 0.7; y = 0, 0.035, 0.05, 0.067) solid solutions were synthesized by mechanical alloying, using commercially available Mg turnings (Merck, purity 99%), Si (< 6 mm, chemPur, purity 99.99%), Sn (< 71 μm, Merck, purity 99.99%) and Sb (5 mm, Alfa Aesar, purity > 99.5%). The precursor elements were weighted according to the targeted nominal stoichiometry, then milled for 4 h until homogeneous powders were obtained using a high energy ball mill (SPEX 8000D Shaker Mill) with stainless steel balls. In order to avoid oxidation and contamination of the powders during synthesis, they were handled in an argon glove box for the complete synthesis. The resulting powders were transferred into a 12.7 mm diameter graphite die and sintered by a direct current sinter press (DSP 510 SE, Dr. Fritsch GmbH) in vacuum (~10^{-5} bar) at a temperature of 973 K for 20 min under a uniaxial pressure of 66 MPa on the die with a heating rate of 1 K/s to obtain compacted pellets. Two $Mg_{1.95}Si_{0.233}Sn_{0.7}Sb_{0.067}$ samples have been sintered from the same powder. They are differentiated as $Mg_{1.95}Si_{0.233}Sn_{0.7}Sb_{0.067}$-I and $Mg_{1.95}Si_{0.233}Sn_{0.7}Sb_{0.067}$-II. $Mg_{1.95}Si_{0.233}Sn_{0.7}Sb_{0.067}$-I was used for low-temperature measurement and $Mg_{1.95}Si_{0.233}Sn_{0.7}Sb_{0.067}$-II for Hall measurement. Both samples have the same properties and microstructure.

Material characterization

The sample density was determined using Archimedes' method with an uncertainty of around 5%. The pellet's microstructure and phase purity were characterized by Scanning Electron Microscopy (SEM) and Energy Dispersive X-ray spectroscopy (EDS) using a Hitachi High Tech's SU3900 SEM device. X-ray diffraction (XRD) patterns of the pellets were obtained using a Bruker D8 device with secondary monochromator, Co-K_α radiation (1.78897 Å) and a step size 0.01° in the 2θ range of 20°-80°. The elemental composition of a single $Mg_{1.95}Si_{0.3}Sn_{0.7}$ sample was determined using Inductively Coupled Plasma Atomic Emission Spectroscopy (ICP-AES)[49-51].

The functional homogeneity of the samples at room temperature was checked by spatial mapping of the Seebeck coefficient using an in-house developed Potential and Seebeck microprobe (PSM) with a spatial

resolution of 50 μm[52,53]. The temperature-dependent electrical conductivity (σ) and Seebeck coefficient (*S*) between room temperature and 723 K were measured using an in-house developed device with a four-probe technique under helium atmosphere, at Deutsches Zentrum für Luft und Raumfahrt (DLR)[54,55]. Low temperature measurements were performed in another home-made apparatuses as described in[56], developed by Parzer *et al.* at TU Wien. As shown in Supplementary Figure 1, it shows good agreement of both Seebeck coefficient and electrical conductivity to high temperature measurement in both cases, with differences < 10% providing evidence on good measurement accuracy. The thermal diffusivity (α) measurement was performed using a laser flash method (Netzsch LFA 427 apparatus) in argon atmosphere. From this, the thermal conductivity (κ) was calculated using $\kappa = \alpha\rho C_p$, where ρ and C_p are the sample density and heat capacity dependent on the composition at constant pressure, respectively. C_p was calculated using the Dulong-Petit limit estimating the specific heat at constant volume (c_V^{DP}) and a thermal expansion correction: $C_P = c_V^{DP} + \frac{9E_t^2 T}{\beta_T \rho}$, $E_t^{Mg_2Si_{0.3}Sn_{0.7}} \sim 1.8 * 10^{-5}$ K^{-1} and $\beta_T^{Mg_2Si_{0.3}Sn_{0.7}} \sim 2.19 * 10^{-11}$ Pa^{-1}where E_t and β_T are the linear coefficient of thermal expansion and isothermal compressibility of $Mg_2Si_{0.3}Sn_{0.7}$ respectively. The electronic thermal conductivity was estimated by the Wiedemann-Franz law by $\kappa_e = L\sigma T$ where L is the Lorenz number, calculated within a single parabolic band (SPB) model from the Fermi integrals $F_i(\eta)$ using

$$L = \left(\frac{k_B}{e}\right)^2 \frac{3F_0(\eta)F_2(\eta) - 4F_1^2(\eta)}{F_0(\eta)^2} \quad (1)$$

The lattice contribution was then determined by subtracting κ_e from the total thermal conductivity $\kappa_{lat} = \kappa - \kappa_e$. The room-temperature Hall coefficient (R_H) for different samples was measured using an in-house facility with a van der Pauw configuration[34,57]. The measurement signals were acquired under varying magnetic fields up to 0.5 T. The Hall carrier concentration n_H was estimated from R_H assuming a single carrier type $n_H = \frac{1}{eR_H}$ where e is the electronic charge. Finally, the weighted mobility μ_w, which is proportional to the thermoelectric quality factor β was calculated with the equation by Snyder *et al.*[58] using our measured Seebeck coefficient and electrical conductivity.

$$\mu_w = \frac{3h^3\sigma}{8\pi e(2m_e k_B T)^{3/2}} \left[\frac{\exp\left[\frac{|S|}{k_B/e} - 2\right]}{1 + \exp\left[-5\left(\frac{|S|}{k_B/e} - 1\right)\right]} + \frac{\frac{3}{\pi^2}\frac{|S|}{k_B/e}}{1 + \exp\left[5\left(\frac{|S|}{k_B/e} - 1\right)\right]} \right] \quad (2)$$

Measurement error uncertainties for *S*, σ, κ and n_H are ± 5%, ± 5%, ± 8% and ± 10%, respectively. Naithani *et al.* studied the associated uncertainty of microscopic parameters derived from a SPB model and due to aforementioned measurement uncertainties relative uncertainties ranging from 5% to 15% for the density of states mass and 12% to 20% for the deformation potential for Seebeck coefficients between 40-400 μV/K can be expected[59].

RESULTS

N-type $Mg_{2-\delta}Si_{0.3-x-y}Sn_xSb_y$ (δ = 0.1, 0.05; x = 0.7; y = 0, 0.035, 0.05, 0.067) samples were synthesized and analyzed in this study. The main characteristic of the synthesized samples is the Mg content being deficient compared to what has been reported on Mg_2(Si,Sn) solid solutions so far and deficient also with respect to the nominal Mg:*X* (*X*= Si,Sn) of 2:1.

The phase purity of the samples was investigated using XRD. The X-ray diffractograms of synthesized Mg-poor undoped and doped samples are represented in Figure 1 in comparison to synthesized Mg-rich material. All diffractograms show the formation of phase-pure material which crystallizes in the *fcc* structure with $Fm\bar{3}m$ space group (sharp peaks, no peak overlapping). The square root of the normalized intensities is plotted to enhance the visibility of potential impurity phases. Moreover, the XRD patterns

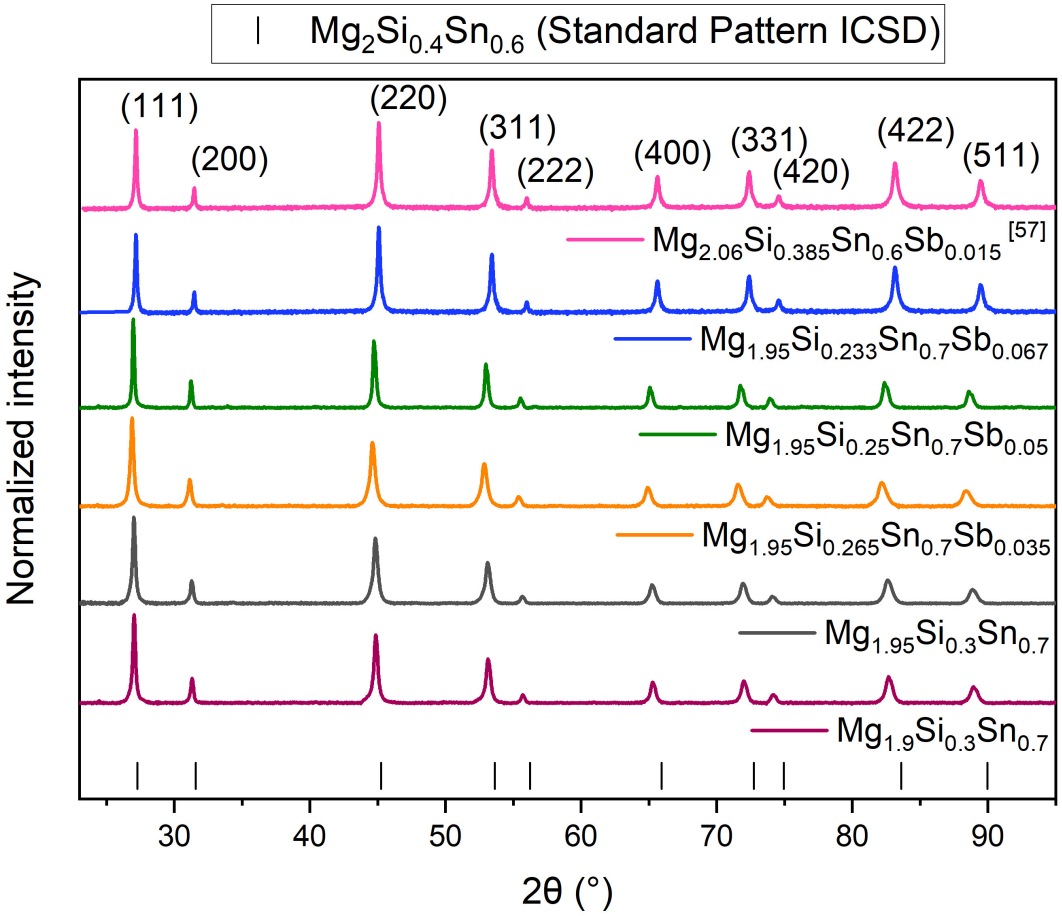

Figure 1. X-ray diffraction diffractogram of samples with varying Mg and Sb composition.

show no obvious peak splitting that would indicate any phase separation of the sample. For some samples a small asymmetry in the XRD peaks is observed, potentially due to variations in the Si:Sn ratio in $Mg_2(Si,Sn)$. The diffractograms of Mg-poor doped samples are comparable to those of Mg-rich doped sample from Sankhla *et al.*[57] that were synthesized using the same route and the same devices.

The obtained lattice parameter of $Mg_{1.95}Si_{0.3}Sn_{0.7}$ (a = 6.643 Å) is in close agreement with literature values of undoped $Mg_2Si_{0.3}Sn_{0.7}$ (a = 6.64 Å[46], 6.62 Å[60], 6.66 Å[61]). The obtained lattice parameter of the $Mg_{1.95}Si_{0.233}Sn_{0.7}Sb_{0.067}$ sample (a = 6.669 Å) is higher than the one of undoped Mg-poor solid solution. A systematic increase of a with Sb content suggests the dopant incorporation in the matrix. Sb is substituting on the X position and no secondary phases such as Sb or Mg_3Sb_2 are observed in the XRD pattern. All densities and lattice parameters are given in Table 1. The weighted residuals of the Rietveld refinement are given in Supplementary Table 1. Examining the sample densities reveals no observable trend in relation to Mg content.

The microstructure of the samples was investigated using SEM combined with EDS to observe possible phase separation due to unmixing of the solid solution[62], to identify secondary phases and to analyze the possible differences originating from the reduced Mg content. For all the synthesized samples, microstructure and phase constitution are very similar, as illustrated in Figure 2. Additional images are provided in the Supplementary Materials [Supplementary Figure 3]. Backscattered electron images done by

Table 1. Sample density and lattice parameter determined by Rietveld refinement for $Mg_{1.9}Si_{0.3}Sn_{0.7}$, $Mg_{1.95}Si_{0.3}Sn_{0.7}$, $Mg_{1.95}Si_{0.233}Sn_{0.7}Sb_{0.067}$, $Mg_{1.95}Si_{0.250}Sn_{0.7}Sb_{0.050}$ and $Mg_{1.95}Si_{0.265}Sn_{0.7}Sb_{0.035}$ samples

	Density (g/cm^{-3})	Lattice parameter (Å)
$Mg_{1.9}Si_{0.3}Sn_{0.7}$	3.10	6.636
$Mg_{1.95}Si_{0.3}Sn_{0.7}$	3.10	6.643
$Mg_{1.95}Si_{0.233}Sn_{0.7}Sb_{0.067}$	3.22	6.669
$Mg_{1.95}Si_{0.250}Sn_{0.7}Sb_{0.050}$	3.23	6.664
$Mg_{1.95}Si_{0.265}Sn_{0.7}Sb_{0.035}$	3.22	6.659
$Mg_{2.06}Si_{0.385}Sn_{0.6}Sb_{0.015}$ [34]	3.00	6.608

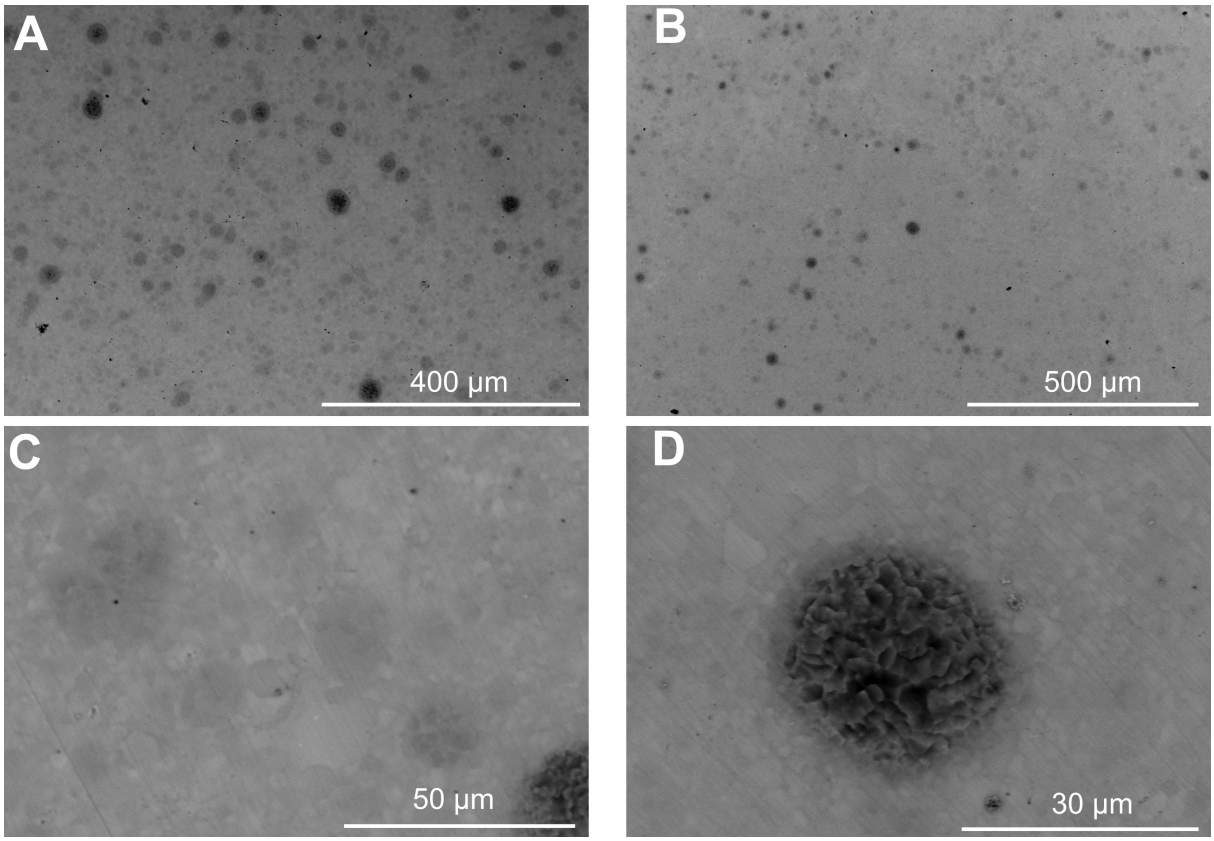

Figure 2. Low and high magnification BSE-SEM images of (A and C) $Mg_{1.95}Si_{0.3}Sn_{0.7}$, (B and D) $Mg_{1.95}Si_{0.233}Sn_{0.7}Sb_{0.067}$. The BSE-SEM images show the microstructure of undoped and doped Mg-poor material. One can see that globular, sub-structured inclusions are visible in both samples. Those inclusions are Si-rich Mg_2X precipitated. Some contrast is also visible in both matrixes. Similar contrast is also visible in Mg-rich material as shown in Figure 2. Such contrast is due to slight Si:Sn variations. EDS mapping of the Si-rich regions are given in Supplementary Figure 2. EDS: Energy dispersive X-ray spectroscopy; BSE-SEM: backscattered electron-scanning electron spectroscopy.

SEM, we do not observe precipitated elemental Si or Sn for any of the samples as might be expected due to the Mg-deficient nominal stoichiometry. Besides, we observe a relatively homogeneous matrix with globular, sub-structured Si-rich Mg_2X inclusions distributed all over the sample [Figure 2D], which are not detected in XRD. This is explained by their low area fraction and variable composition which leads to small and smeared signals. Furthermore, such Si-rich Mg_2X regions are not due to unmixing but rather a consequence of an incomplete reaction, as is typical for this material system when prepared by ball milling[27,34,57], which originate probably from the relatively slow dissolution of Si into Mg_2X during milling

and sintering[31,63]. As shown in Supplementary Figure 4, when comparing as-sintered and annealed SEM/EDS images of $Mg_{1.95}Si_{0.3}Sn_{0.7}$ sample, one can clearly see that the Si-rich Mg_2X regions are dissolving in the matrix. As we know that having such Si-rich regions will dissolve with time and do not impact the thermoelectric material properties, we remain with the current, optimized synthesis route. Finally, no secondary phases containing Sb are observed for the doped sample, implying good incorporation of the dopant into the host structure. As shown by Nolas *et al.*[47], Mg_2Si can dissolve up to 37 mol.% of Sb. According to our results, we believe that Sb solubility limit in $Mg_2Si_{1-x}Sn_x$ with x~0.3 is above 6.7 mol.% as no Sb impurities were detected in the samples.

Inductively coupled plasma atomic emission spectroscopy (ICP-AES) has been performed on a $Mg_{1.95}Si_{0.3}Sn_{0.7}$ for a more accurate quantification of the respective elements. Such measurements have a high reliably, leading to low standard deviations (less than 1 at.%) as demonstrated by Ai *et al.*[64] and He *et al.*[65]. We obtain Mg = 66.68 at.%, Si = 10.23 at.% and Sn = 23.09 at.%, while according to the nominal composition, Mg = 66.1 at.%, Si = 10.17 at.% and Sn = 23.73 at.% are expected. The measured values correspond to a nominal stoichiometry of $Mg_{2.001}Si_{0.307}Sn_{0.693}$, where the content of Si + Sn was normalized to unity. Essentially, the ICP measurement reveals a Mg:X (X: Si,Sn) ratio quite close to 2:1, even though the material was synthesized with a 2.5% deficiency of the Mg content. Furthermore, we also see a small, but measurable increase of Si:Sn with respect to the starting composition. Indeed, if we quantify how much Sn is missing compared to the nominal Si:Sn ratio, it amounts to 2.2% of the overall X component which almost exactly balances the nominal Mg under-stoichiometry.

The main carrier type and functional homogeneity of $Mg_{1.95}Si_{0.3}Sn_{0.7}$ and $Mg_{1.95}Si_{0.233}Sn_{0.7}Sb_{0.067}$ was determined by a room temperature surface Seebeck coefficient mapping using a PSM as shown in Figure 3A and B. The Seebeck coefficient spatial map is showing n-type conduction for Mg-poor undoped and doped material, respectively. The Seebeck coefficient obtained by PSM measurement matches with the bulk Seebeck coefficient measured at room temperature using the temperature-dependent in-house developed device [Figure 3A] when assuming an usual underestimation between 10% and 20% of the measured values in the PSM due to the cold finger effect[66]. The functional homogeneity is quantified by a frequency distribution of the Seebeck coefficient distribution profile [Supplementary Figure 5]. The full width half maximum values are 15% and 4% for the undoped and doped sample, respectively. This indicates that the doped sample exhibits better functional homogeneity than the undoped one, plausibly because the Seebeck coefficient is more sensitive to small variations in charge carrier concentration due to local compositional fluctuations at low carrier concentration levels. We also observe a gradient across the sample, potentially due to a slightly inhomogeneous temperature profile during sintering[46] but the difference is around 5% across the whole sample and hence doesn't occlude interpretation of the bulk measurements.

The temperature-dependent transport properties of the samples $Mg_{1.9}Si_{0.3}Sn_{0.7}$, $Mg_{1.95}Si_{0.3}Sn_{0.7}$, $Mg_{1.95}Si_{0.233}Sn_{0.7}Sb_{0.067}$-I, $Mg_{1.95}Si_{0.233}Sn_{0.7}Sb_{0.067}$-II, $Mg_{1.95}Si_{0.25}Sn_{0.7}Sb_{0.05}$ and $Mg_{1.95}Si_{0.265}Sn_{0.7}Sb_{0.035}$ in comparison to a synthesized Mg-rich doped solid solution $Mg_{2.06}Si_{0.385}Sn_{0.6}Sb_{0.015}$ by Sankhla *et al.*[57] are shown in Figure 4. Transport properties of the solid solution samples measured in the heating and cooling mode may differ for the first measured cycle[46], therefore cooling data are plotted here. Both the temperature-dependent Seebeck coefficient and electrical conductivity of the undoped sample exhibit a typical semiconductor behavior while doped samples behave similar to heavily doped semiconductors. The temperature-dependent Seebeck coefficients of all samples plotted in Figure 4A are negative, indicating n-type-dominated conduction in agreement with the surface Seebeck scans [Figure 3]. The two undoped Mg-poor samples ($Mg_{1.95}Si_{0.3}Sn_{0.7}$ and $Mg_{1.9}Si_{0.3}Sn_{0.7}$) have very similar Seebeck coefficients, indicating nearly identical charge carrier concentration, in particular as the Seebeck coefficient is very sensitive to the carrier concentration for low

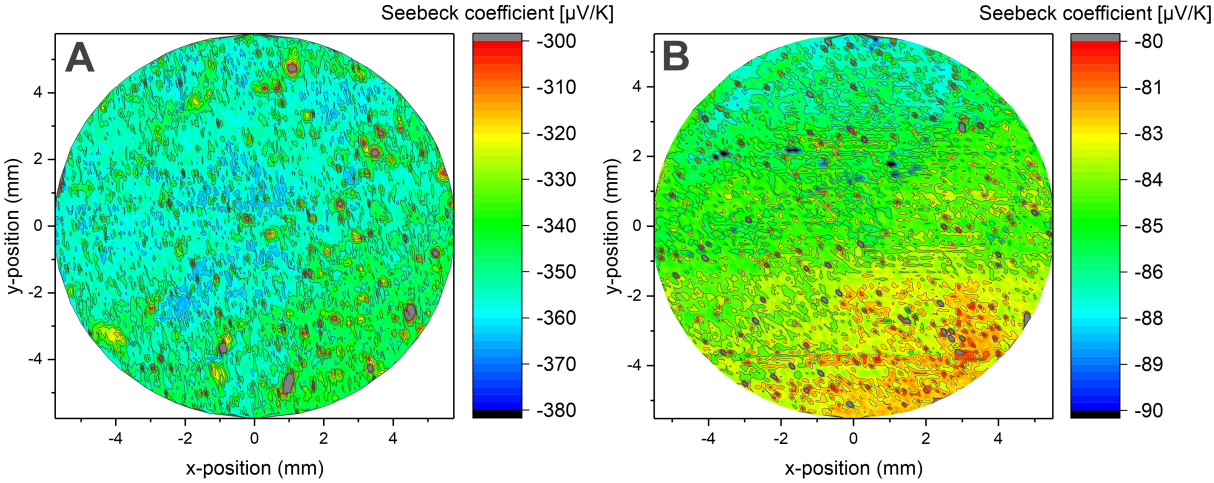

Figure 3. Surface Seebeck map of (A) $Mg_{1.95}Si_{0.3}Sn_{0.7}$ and (B) $Mg_{1.95}Si_{0.233}Sn_{0.7}Sb_{0.067,}$ respectively, measured by the Seebeck microprobe. The scaling of the spot structure where S is outside the matrix range is the same as the Si-rich inclusions visible in the SEM micrographs. SEM: Scanning electron microscopy.

n. This in turn indicates that the intrinsic defect density is very similar for both samples, which makes it plausible that the samples are indeed Mg-poor and not in some intermediate state with respect to Mg content. Undoped Mg-poor solid solutions are expected to exhibit weaker n-type behavior (lower carrier concentration and larger n-type Seebeck) compared to undoped Mg-rich Mg_2(Si,Sn), due to a larger density of Mg vacancies, which act as acceptor defects, and lower densities of donating Mg interstitials, both changes reducing the number of free electrons. Supplementary Figure 6 shows the carrier concentration mapping (obtained using 2PB band modeling using Seebeck coefficient values) for undoped Mg-rich and Mg-poor Mg_2(Si,Sn) with $n \approx 1.3 \times 10^{25}$ m^{-3} for both samples, indicating a larger variation in carrier concentration for Mg-rich material ($\Delta n_{\text{Mg-poor}} = 0.08 \times 10^{25}$ $m^{-3} < \Delta n_{\text{Mg-rich}} = 0.3 \times 10^{25}$ m^{-3}, where Δn represents the respective standard deviation). The exact reason for this remains to be confirmed, but the result might be interpreted as stronger variation in carrier concentration due to locally varying, beginning Mg-loss of the Mg-rich sample.

Thermal excitation of the minority charge carriers is clearly visible for the undoped sample ($Mg_{1.95}Si_{0.3}Sn_{0.7}$) at high temperatures as the (absolute) Seebeck coefficient starts decreasing. Such behavior is also visible in $Mg_{1.95}Si_{0.265}Sn_{0.7}Sb_{0.035}$ when excitation of the minority carriers is visible at temperatures over 650 K. In contrast, samples highly doped with Sb (y = 0.05, 0.067) exhibit a linear trend, suggesting that the Seebeck coefficient is dominated by the majority carriers. The trend of the electrical conductivity is opposite to the behavior of the Seebeck coefficient, with a higher variance in amplitude. In contrast to the observations by Kato *et al.*[67] and Sankhla *et al.*[57], grain boundary scattering is barely visible for the Mg-poor samples. A maximum power factor of 43.3 $\mu W cm^{-1} K^{-2}$ at 640 K was achieved for $Mg_{1.95}Si_{0.233}Sn_{0.7}Sb_{0.067}$.

Besides this, for undoped samples, the temperature dependent thermal conductivity [Figure 4C] first decreases with increasing temperature as expected and then increases due to the bipolar effect for temperatures above 473 K. The thermal conductivity increases by adding Sb due to the larger electronic contribution. The combined lattice and bipolar contribution [Figure 4D] of the undoped sample shows a sharp increase above 500 K which is due to the bipolar contribution. However, for the doped sample, the lattice thermal conductivity is greatly reduced compared to undoped samples. The high power factor and low thermal conductivity of $Mg_{1.95}Si_{0.233}Sn_{0.7}Sb_{0.067}$ lead to a relatively high experimental figure of merit of 1.2 ± 0.16 at 719 K [Figure 4F].

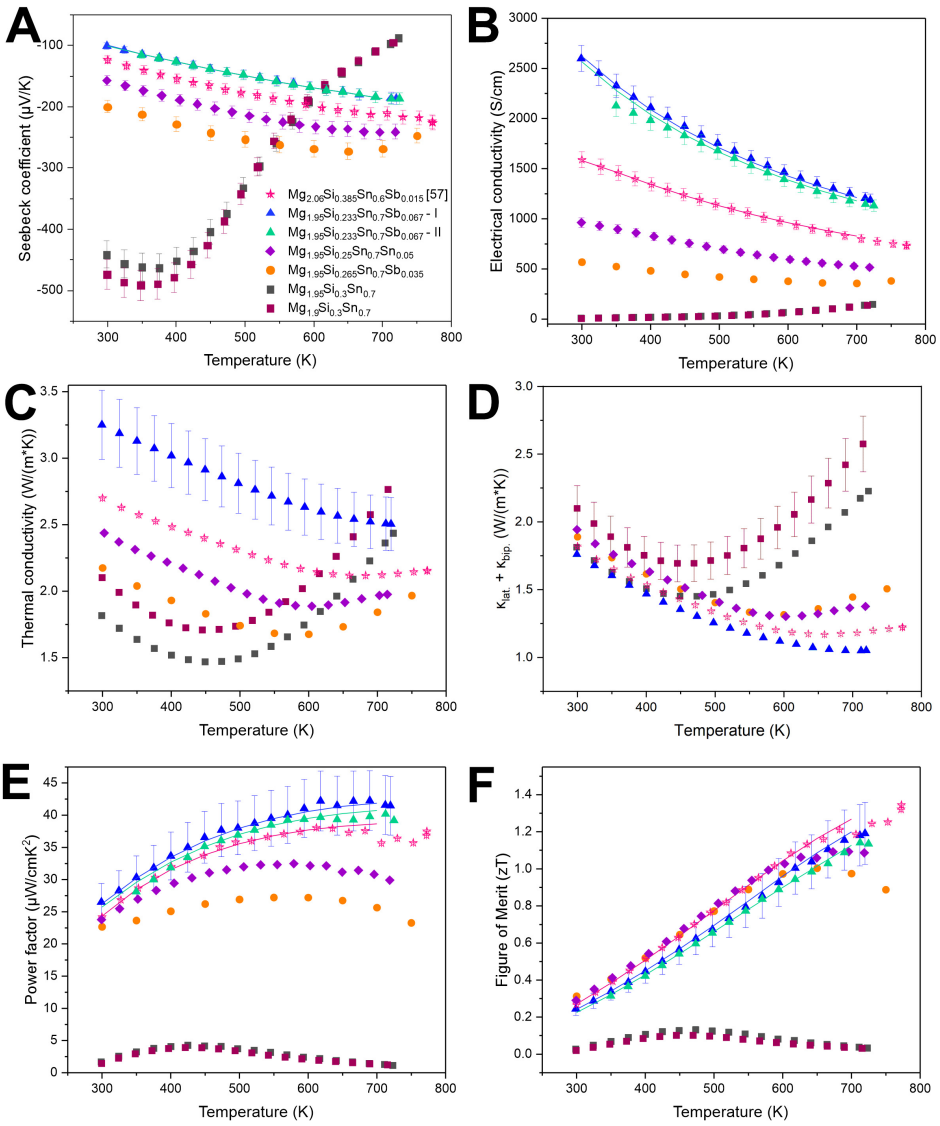

Figure 4. Experimental (filled symbols) and simulated (solid lines) temperature dependent (A) Seebeck coefficient, (B) electrical conductivity, (C) thermal conductivity, (D) lattice and bipolar thermal conductivity, (E) power factor and (F) figure of merit for different doping and Mg concentrations for $Mg_{2-\delta}Si_{0.3-y}Sn_{0.7}Sb_y$. Theoretical results were obtained from a single parabolic band (SPB) model. Only samples where the Hall effect was measured, were modelled. For some samples, the height of the error bars is lower than the size of the symbol, hence not visible.

Regarding the samples with lower dopant concentrations (y = 0.035 and y = 0.05), zT values are higher than the highly doped sample at temperatures from room temperature to 600 K. These values are comparable to zT values of the Mg-rich reference sample. The decrease in zT at higher temperatures is attributed to the influence of minority charges. Overall, the power factor is highest for y = 0.067, followed by the Mg-rich sample, with y = 0.05 showing better properties than y = 0.035. Therefore, the choice between y = 0.05 or y = 0.067 dopant content will depend on the specific application temperature requirements.

DISCUSSION

To prevent material degradation, coatings were initially explored. Focused research has been conducted on coatings, yet no suitable coating has been found for this material system[68-71]. First of all, the typical

mismatch in the coefficient of thermal expansion presents significant challenges when oxides are employed, particularly under thermal cycling. Furthermore, elemental Mg, which drives material degradation is highly reactive. Consequently, many oxides such as Al_2O_3 that have a lower formation enthalpy than MgO might not work as a coating in the long run, as demonstrated by Deshpande *et al.*[72]. Therefore, in our work, we propose the synthesis of Mg-poor materials to prevent direct Mg loss, addressing the degradation mechanism described by Sankhla *et al.*[34], Duparchy *et al.*[27] and Ghosh *et al.*[35].

The synthesis of Mg-poor $Mg_{1.95}Si_{0.3}Sn_{0.7}$ has been successful, leading to the formation of a typical n-type semiconductor. The microstructural analysis proves that no elemental Si or Sn remains; only Si-rich secondary phases within the solid solution system Mg_2(Si,Sn) were formed [Figure 2]. Furthermore, the synthesized Mg-poor sample do not show any Mg_2Si and Mg_2Sn unmixing. These findings contradict the speculation that Mg deficiency initiates unmixing of the solid solution, raised by Yasseri *et al.*[63]. ICP analysis was conducted to determine the elemental composition of the undoped $Mg_{1.95}Si_{0.3}Sn_{0.7}$ sample, resulting in a composition of $Mg_{2.001}Si_{0.307}Sn_{0.693}$, close to Mg_2(Si,Sn), with a higher Mg and lower Sn content than the nominal one. We propose that these differences between nominal and measured composition are the consequence of a self-adjusting stoichiometric balance during the synthesis process, in particular, during uniaxial hot pressing. Indeed, according to the Mg-Si-Sn phase diagram[73], a sample that contains more Sn than the Sn-rich limit according to the miscibility gap[62,73] and is Mg deficient, is located in a three-phase region, with elemental Si, Sn-rich Mg_2X and liquid Mg-Sn (for temperatures above ~210 °C) as coexisting phases. According to the phase diagrams provided in Figure 9 from the work by Orenstein *et al.*[73], $Mg_{1.95}Si_{0.3}Sn_{0.7}$ is not located inside the Sn-rich Mg_2X phase, but we note that our samples have been sintered at 700 °C, i.e., larger than the temperatures at which the ternary isothermal phase diagrams are known and point out that the miscibility gap closes with increasing temperature, and, secondly that Mg_2X samples have been synthesized repeatedly as single-phase materials inside the thermodynamically predicted miscibility gap, presumably due to stabilization by coherent interfaces[63,74]. It is therefore highly plausible that the sintering step leads to the formation of Mg_2(Si,Sn) and Mg-Sn, with the latter being expelled during the pressure-assisted sintering as it is liquid. We do not observe elemental Si (see Figure 2). As Mg_2Si is tighter bound than Mg_2Sn, Si might replace Sn in the structure as long as there is *X* excess. According to the suggested procedure, one would expect a sample with reduced Sn content (as observed) and at the lower solubility limit of Mg in $Mg_{2(1+\delta_1)}X$. The very similar Seebeck data for the two undoped sample supports this. The ICP results with a Mg content slightly larger than 2 is not a contradiction to the sample composition corresponding to the lower solubility limit of Mg but a result of the limited accuracy of the measurement and an indication that the phase width with respect to Mg is smaller than the accuracy of the ICP measurement. For undoped materials, we are not aware of any report on the phase width, but for doped Mg_2X a value of $\Delta\delta_{Mg} = 0.008$ was reported, smaller than typical uncertainties of less than 1 at.% for ICP[64].

All three Mg-poor doped samples were examined by XRD and SEM/EDS [Figures 1 and 2], demonstrating successful dopant incorporation, as no visible Sb-rich phase precipitated were detected. Furthermore, Seebeck coefficient measurements [Figure 3] revealed differences in the Seebeck coefficient between undoped $Mg_{1.95}Si_{0.3}Sn_{0.7}$ and doped $Mg_{1.95}Si_{0.233}Sn_{0.7}Sb_{0.067}$ (-350 μV/K *vs.* -80 μV/K). These observations suggest that Sb was effectively incorporated on the Si/Sn site, with the doped sample exhibiting relatively low local functional fluctuations. The thermoelectric properties of the Mg-poor material improve significantly with doping, resulting in a high power factor and an overall figure of merit comparable to that of Mg-rich material compounds[57] [Figure 4F]. Also, samples $Mg_{1.95}Si_{0.233}Sn_{0.7}Sb_{0.067}$ - I and II are very similar microstructure- and property-wise, indicating a high reproducibility of the synthesis route. Indeed, while the charge carrier concentration for Mg-rich samples might depend on the details of the sintering step (temperature, duration)[31,57] due to Mg loss, using Mg-poor materials might lead to a very high

reproducibility as no excess or loosely bound Mg is lost during the sintering step.

We have calculated the effective doping efficiency (η_{dop}) [Table 2] of Sb from the (measured) carrier concentration n and the nominal dopant concentration under the assumption that each Sb atom replaces one Si/Sn atom and provides one electron, using $\eta_{dop} = \frac{n}{c_{Sb}}$ with $c_{Sb} = \frac{4*y}{a^3}$ the dopant concentration. The effective doping efficiency is much lower for the synthesized Mg-poor samples than for the synthesized Mg-rich materials, which could be caused by Sb becoming electrically inactive (i.e., does not act as a donor anymore). However, if this was the case, comparing the different Mg-poor samples we should see an increase of the doping efficiency with decreasing Sb content, which is not observed. Also, density functional theory (DFT) calculations from Ayachi *et al.*[75] indeed show a change from +1 to neutral for Sb_{Si} and Sb_{Sn} for high Fermi levels (i.e., large carrier concentrations), but these charge transition levels are similar for Mg-rich and Mg-poor materials, hence, Sb becoming inactive is probably not the reason for the decrease in doping efficiency. A more plausible reason could be the formation of compensating defects with increasing Sb content. This has been observed by Kato *et al.*[29] and Dasgupta *et al.*[48] who showed experimentally that Mg vacancies increase with increasing Sb doping, for nominal Mg-rich samples. Also for Mg-poor samples an increase of p-type Mg vacancies is expected with increasing carrier concentration caused by increasing Sb content, leading to a partial compensation of the free electrons from Sb addition.

The transport data of $Mg_{1.95}Si_{0.233}Sn_{0.7}Sb_{0.067}$-II (sample on which Hall measurement was performed) were investigated for differences in the microscopic material parameters using a single parabolic Band (SPB) model with respect to previously reported data for Mg-rich samples and those extracted from the samples after annealing, i.e., presumably Mg-poor[57]. This composition was chosen as it leads to the best thermoelectric performance in the material. As no thermal conductivity measurements were performed on that sample, the data of $Mg_{1.95}Si_{0.233}Sn_{0.7}Sb_{0.067}$-I (with almost identical electrical properties) was utilized instead.

The SPB model can be used for highly doped samples of $Mg_2Si_{1-x}Sn_x$ with x~0.7 due to this composition being closely located to convergence of CBs, as described in detail in many studies[21,57,76,77]. In our case we used $x = 0.7 + y$ with y being the Sb content (Sb is comparable in size to Sn rather than Si). The basic parameters of this model are the reduced chemical potential (η), the mobility parameter (μ_0) and the density of states effective mass (m_D^*), governed by

$$S(\eta) = \frac{k_B}{e}\left(\frac{2F_1(\eta)}{F_0(\eta)} - \eta\right) \tag{3}$$

$$n = 4\pi\left(\frac{2m_D^* k_B T}{h^2}\right)^{\frac{3}{2}} F_{\frac{1}{2}}(\eta) \tag{4}$$

$$n_H = \frac{n}{r_H}, r_H = \frac{1.5F_{\frac{1}{2}}(\eta)F_{-\frac{1}{2}}(\eta)}{F_0^2(\eta)} \tag{5}$$

$$\mu_H = \mu_0 \frac{F_{-\frac{1}{2}}(\eta)}{2F_0(\eta)} \tag{6}$$

$$\sigma = n_H e \mu_H \tag{7}$$

Here k_B represents Boltzmann's constant, h is Planck's constant, and $F_i = \int_0^\infty \frac{\varepsilon^i d\varepsilon}{1+\exp[\varepsilon-\eta]}$ are the Fermi integrals of the order of i, and the reduced chemical potential η is given by $\eta = \frac{E_F}{k_B T}$ where E_F is the Fermi level. For the calculation we have assumed a scattering parameter of $\lambda = 0$ corresponding to the energy dependence of scattering with acoustic phonons (AP) and alloy scattering (AS)[78,79].

Table 2. Charge carrier concentration, nominal dopant concentration and effective doping efficiency of synthesized Mg-poor and Mg-rich doped samples. The charge carrier concentration of both $Mg_{1.95}Si_{0.25}Sn_{0.7}Sb_{0.05}$ and $Mg_{1.95}Si_{0.265}Sn_{0.7}Sb_{0.035}$ were estimated using the same effective mass as for $Mg_{1.95}Si_{0.233}Sn_{0.7}Sb_{0.067}$

	n (10^{20} cm^{-3})	c_{Sb} (10^{20} cm^{-3})	η_{dop}
$Mg_{1.95}Si_{0.233}Sn_{0.7}Sb_{0.067}$	2.71	9.03	0.30
$Mg_{1.95}Si_{0.25}Sn_{0.7}Sb_{0.05}$	1.12	6.76	0.17
$Mg_{1.95}Si_{0.265}Sn_{0.7}Sb_{0.035}$	0.63	4.75	0.13
$Mg_{2.06}Si_{0.385}Sn_{0.6}Sb_{0.015}$ [34]	2.20	2.08	1.06

Using the room temperature Hall coefficient, we calculate the density of states effective mass as function of temperature assuming the carrier concentration to be constant and corresponding to the room temperature value. Figure 5A shows that the density of states effective mass is constant over temperature, verifying the validity of the SPB model here without considering any contribution from the valence band (VB) or a second CB. The room temperature charge carrier concentration (n_H), the Hall mobility (μ_H) and the density of states effective mass (m_D^*) of $Mg_{1.95}Si_{0.233}Sn_{0.7}Sb_{0.067}$-II from this work and various other samples from the literature[57], namely $Mg_{2.06}Si_{0.385}Sn_{0.6}Sb_{0.015}$ before Mg loss, $Mg_{2.06}Si_{0.385}Sn_{0.6}Sb_{0.015}$ after intermediate Mg loss and $Mg_{2.06}Si_{0.385}Sn_{0.6}Sb_{0.015}$ after Mg loss - fully Mg depleted, are summarized in Table 3.

The Hall mobilities for Sample 1 [Mg-poor] and Sample 2 [Mg-rich] are roughly comparable as shown in Figure 5B. with the Sample 1 [Mg-poor] showing slightly higher mobilities. This is potentially due to larger Sn content in that sample, leading to slightly reduced Alloy scattering. Notably, we do not observe a reduced mobility of the Sample 1 [Mg-poor], in contrast to results from Kato *et al.*[67] who observed that Mg-poor doped Mg_2Si have a lower Hall mobility than Mg-rich Mg_2Si. The weighted mobilities exhibit a similar behavior as the Hall mobilities, in line with similar density of states effective mass and hence electronic band structure between the samples. Finally, a higher weighted mobility indicates higher achievable power factor for Sample 1 [Mg-poor] compared to Sample 2 [Mg-rich].

While the Hall mobility (μ_H) is affected by the carrier concentration, the mobility parameter (μ_0) is used for scattering analysis to understand the differences in carrier mobility as independent of carrier density. We modelled μ_0 making use of the low and high temperature conductivity measurement by considering scattering processes of charge carriers with acoustic phonons, lattice disorder due to alloy scattering and grain boundaries. Indeed, acoustic phonon scattering is the most relevant scattering mechanism for highly doped samples at high temperatures[80]. Alloy scattering is included as it is a relevant mechanism in solid solutions[78]. Grain boundary scattering has been shown to be relevant in several Mg-based TE materials[81-83] especially for samples that have experienced Mg-loss[34,84]. We assume that the scattering mechanisms are independent of each other meaning that the mobilities follow Matthiessen's rule[76]:

$$\frac{1}{\mu_0} = \frac{1}{\mu_0^{AP}} + \frac{1}{\mu_0^{AS}} + \frac{1}{\mu_0^{GB}} \tag{8}$$

The acoustic phonon scattering term (μ_0^{AP}) is given by

$$\mu_0^{AP} = \frac{\pi\sqrt{8}e\hbar^4\rho v_l^2}{4E_{Def}^2(m_s)^{2.5}(k_BT)^{1.5}} \tag{9}$$

where $\hbar$ is the reduced Plank constant, ρ is the theoretical mass density, v_l is the longitudinal velocity of sound (7,680-2,880x m^{2}s^{-1} for $Mg_2Si_{1-x}Sn_x$), E_{Def} is the deformation potential, which characterizes the interaction between charge carriers and phonons. The single valley effective mass m_s is obtained from

Table 3. Nominal composition, sample labelling, room temperature charge carrier concentration n_H, Hall mobility μ_H at room temperature and density of states effective mass of $Mg_{1.95}Si_{0.233}Sn_{0.7}Sb_{0.06}$-II and Mg-rich doped samples before and after Mg loss from Sankhla *et al.*[57]

Nominal composition	Sample labelling	$n_H \times 10^{20}$ (cm^{-3})	μ_H (cm^2/Vs)	(m_0)
$Mg_{1.95}Si_{0.233}Sn_{0.7}Sb_{0.067}$	Sample 1 [Mg-poor]	2.5	52.3	2.1
$Mg_{2.06}Si_{0.385}Sn_{0.6}Sb_{0.015}$ before Mg loss	Sample 2 [Mg-rich]	2.0	49.2	2.4
$Mg_{2.06}Si_{0.385}Sn_{0.6}Sb_{0.015}$ after intermediate Mg loss	Sample 2 [after Mg loss]	1.5	41.0	2.4
$Mg_{2.06}Si_{0.385}Sn_{0.6}Sb_{0.015}$ after Mg loss - fully Mg depleted	Sample 2 [Mg-depleted]	0.3	-	1.8

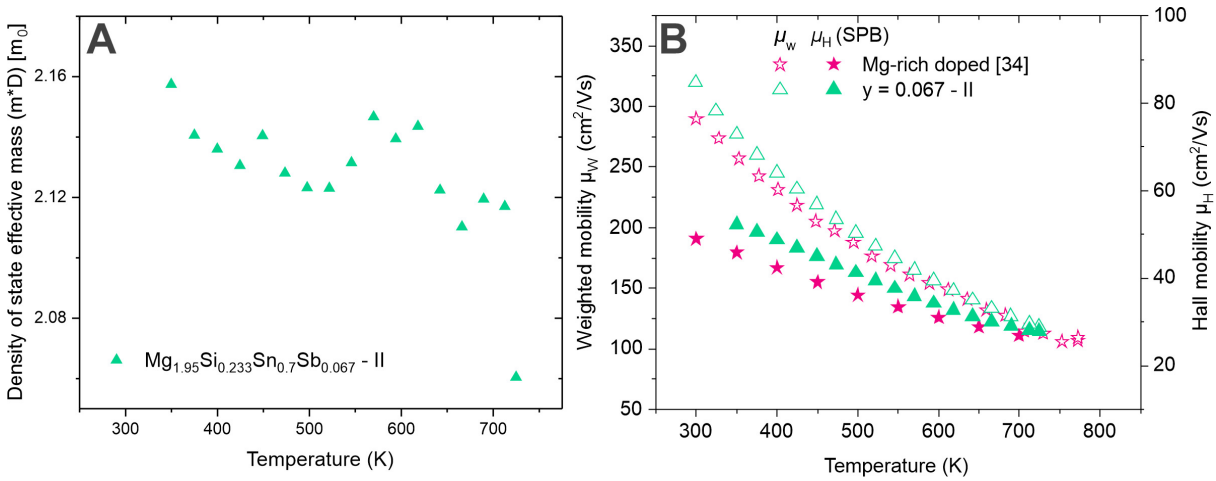

Figure 5. (A)Density of states effective mass as a function of temperature for the $Mg_{1.95}Si_{0.233}Sn_{0.7}Sb_{0.067}$-II sample. The effective mass was obtained from room temperature Hall measurement, assuming a constant carrier concentration; (B) Weighted mobility (μ_w) and Hall mobility (μ_H) of $Mg_{2.06}Si_{0.385}Sn_{0.6}Sb_{0.015}$ and $Mg_{1.95}Si_{0.233}Sn_{0.7}Sb_{0.067}$-II.

$m_s = (\frac{m_D^*}{N_V^{2/3}})$, with $N_V = 6$.

The alloy scattering mobility (μ_0^{AS}) is given by:

$$\mu_0^{AS} = \frac{16e\hbar N_0}{3\,2^{1.5}\pi x(1-x)E_{AS}^2(m_s)^{2.5}(k_BT)^{0.5}} \tag{10}$$

with N_0 being the number of atoms per unit volume, x being the Sn + Sb fraction at the X site and E_{AS} the alloy scattering potential.

Last but not least, the mobility constant of grain boundary scattering (μ_0^{GB}) is defined by:

$$\mu_0^{GB} = Be\left(\frac{1}{2\pi m_s k_B T}\right)^{1/2}\exp\left(\frac{-E_B}{k_B T}\right) \tag{11}$$

where B is the grain size, which is kept constant (B = 5 μm)[57] and E_B is the potential barrier at the grain boundary (called barrier height).

Using E_{AS} = 0.5 eV from literature, E_{Def} and E_B as remaining temperature-independent unknowns can be extracted by fitting the modeled mobility parameter to the "experimental" $\mu_0 = \mu_H \left(\frac{F_{-1}(\eta)}{2F_0(\eta)}\right)^{-1}$. Doing so we obtain E_{Def} =11 eV [Figure 6], a deformation potential constant similar to those extracted from modelling the mobility of Sample 2 [Mg-rich] (E_{Def} = 9.8 eV) and Sample 2 [after Mg loss] (11 eV) extracted from Sankhla *et al.* study[57]. Liu *et al.*[76] demonstrated high mobility of Mg-rich $Mg_2(Si,Sn)$ due to the low deformation potential varying between 8.77 and 9.43 eV, while Agrawal *et al.*[85] found a deformation potential of 9.32 eV, both being comparable to what was obtained for Mg-poor $Mg_2(Si,Sn)$ in this study. This difference of ~10% in the deformation potentials could be easily attributed to experimental uncertainty[59], confirming that there is no significant difference between Mg-rich and our Mg-poor material.

The low temperature electrical resistivity data presented in Figure 6 were used for the mobility parameter analysis. Indeed, one would expect a convex increase at the left-hand curvature due to grain boundary scattering which is not really the case. Fitting the mobility data down to 150 K, we estimate a barrier height for grain boundary scattering of E_B = 60 meV, significantly below values extracted from Sankhla *et al.*[57] who obtained E_B = 100 meV for Sample 2 [Mg-rich], which increased to E_B = 131 meV after experiencing some Mg loss {Sample 2 [after Mg loss]}. For Sample 2 [Mg-depleted] an even higher barrier height was indicated by the positive slope of σ(T)[34]. Modelling results with these barrier heights are shown in Figure 6, showing that barrier heights extracted from Sample 2 [Mg-rich] predict a stronger mobility reduction towards low temperatures than is observed for Sample 1 [Mg-poor]. In combination with the absence of indications for grain boundary scattering for all Mg-poor samples of this study [Figure 4], we can rule out a large impact of grain boundary scattering for the here synthesized Mg-poor samples, in contrast to observations on Sample 2 [Mg-rich], and particularly to Sample 2 [after Mg loss]. Note that the employed model is inadequate to model mobilities at very low temperatures as Equation (9) forces the total mobility to 0 for any finite barrier height for temperature towards 0.

Overall, with respect to the SPB parameters, Sample 2 [after Mg loss] and Sample 2 [Mg-depleted] show a clear trend of decreasing mobility, increasing GB scattering and increasing deformation potential with Mg-loss while Sample 1 [Mg-poor] is parameter-wise relatively close to Sample 2 [Mg-rich]. An important finding is that synthesized Sample 1 [Mg-poor] has not the same properties as the by annealing Sample 2 [Mg-depleted].

The low impact of grain boundary scattering in the synthesized Mg-poor material is a crucial finding, proving that synthesized Mg-poor materials are comparable to Sample 2 [Mg-rich] reported in the literature and clearly different than Sample 2 [Mg-depleted] which was initially Mg-rich. Our data for Sample 1 [Mg-poor] clearly show that substantial grain boundary scattering is not related to the Mg content as such. Instead, it might be explained by several reasons. First of all, it could be that it is not the composition that determines the effect of the grain boundaries but rather different grain boundary nature. In the case of Mg-depletion, many Mg vacancies form towards the grain boundaries, disturbing the transport while for synthesized Mg-poor sample, the grain boundaries could be Si/Sn rich from the self-adjusting synthesis, leading to less vacancies. Second, de Boor *et al.*[86] attributed grain boundary scattering to MgO formation and observed a correlation between MgO content and barrier height, for Mg_2Si that was nominally Mg-rich. Such MgO will only form rapidly if excess Mg is available in the material. Finally, such low impact of grain boundary scattering could be explained by a different Si to Sn content at the grain boundaries between synthesized Mg-poor and Mg-depleted samples which could influence the barrier height.

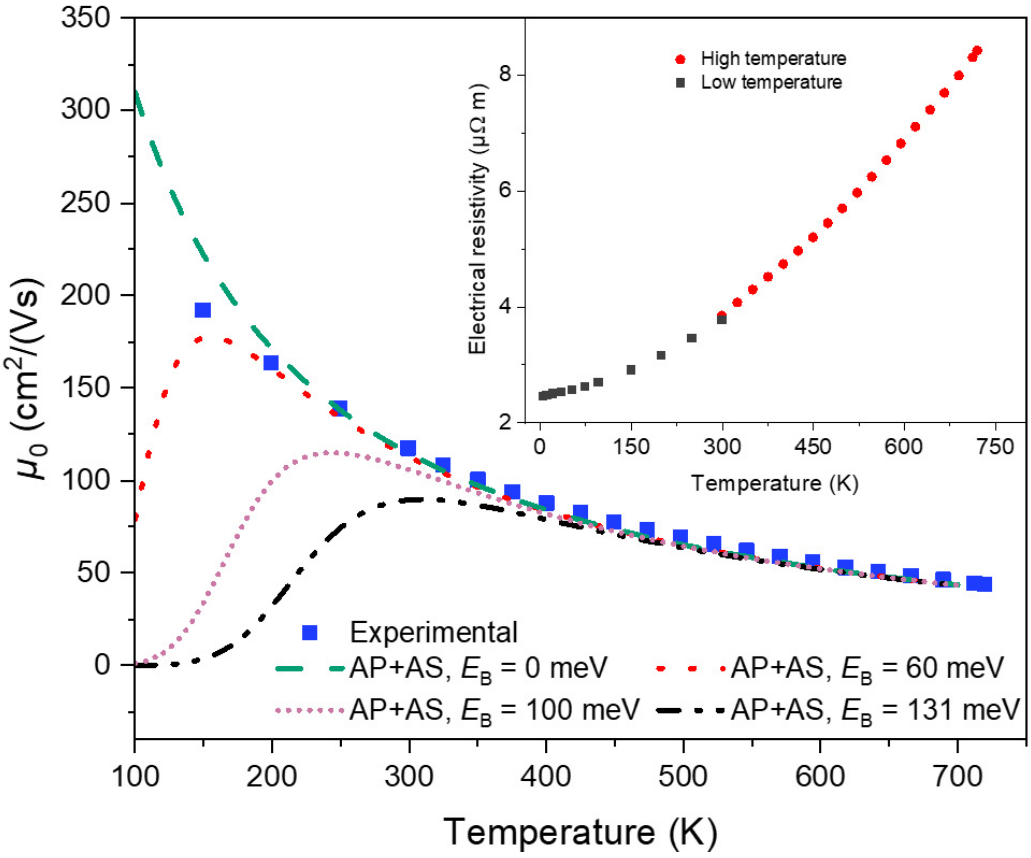

Figure 6. Comparison between experimental and calculated mobility parameter assuming acoustic phonon scattering, alloy scattering and grain boundary scattering for the sample $Mg_{1.95}Si_{0.233}Sn_{0.7}Sb_{0.067}$-I. The deformation potential was set at 11 eV, the alloy scattering potential at 0.5 eV and the results for four different barrier heights are shown: 0 meV (no GB scatter), 100 meV and 131 meV (reference values, used by Sankhla *et al.*[57] in their study) and 60 eV, resulting in a good fit to the experimental data. The inset represents merged low-temperature data and high temperature data of electrical conductivity of $Mg_{1.95}Si_{0.233}Sn_{0.7}Sb_{0.067\text{-I}}$. The low-temperature data were fitted to the high-temperature ones with a constant factor assuming device uncertainty of 10% to fit the high temperature data for further modeling of the scattering parameters.

The thermoelectric figure of merit for a material that can be determined by an SPB model can be written as $zT = \frac{S^2}{L+(\psi\beta)^{-1}}$ with $\psi = \frac{8\pi e}{3}\left(\frac{2m_0 k_B}{h^2}\right)^{1.5} F_0$ and the material quality factor $\beta = \frac{\left(\frac{m_D^*}{m_0}\right)^{1.5}\mu_0 T^{2.5}}{\kappa_{lat}}$. This material quality factor β, unlike the figure of merit, can be used to evaluate the potential thermoelectric performance of a TE compound independently of whether the optimum carrier concentration has been adjusted as β is independent of the carrier concentration[57,58,87]. The $Mg_{1.95}Si_{0.233}Sn_{0.7}Sb_{0.067}$ sample exhibits more or less the same material quality factor β as the Mg-rich materials from the literature [Figure 7A] while a lower material quality factor was extracted for Mg-rich materials after experiencing Mg loss. From the $zT(n)$ curve plotted in Figure 7B, for a Mg-poor doped sample in comparison to Mg-rich doped (with and without Mg loss), it is indicated that the charge carrier concentration is not yet optimized using an Sb dopant concentration of 6.7% for the Mg-poor materials, and an increase up to $zT \approx 1.4$ at 700 K might be achievable with a lower doping content. On the other hand, it is also well-known that the SPB model overestimates zT significantly towards lower carrier concentrations as it ignores the impact of the minority carriers. Indeed, the samples with lower dopant concentrations (y = 0.035, 0.05) show a reduced figure of merit, which can be understood from the onset of minority carrier effects above 600 K in the Seebeck coefficient and the thermal conductivity. While a two or three band model would be required for a quantitative assessment, we deduce that only a small increase of zT by further adjusting the carrier

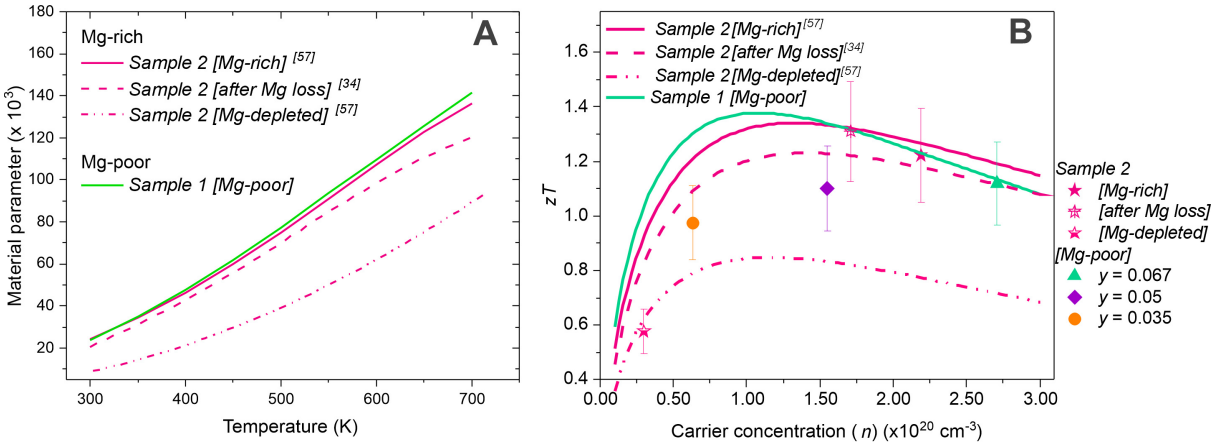

Figure 7. (A) Predicted temperature-dependent material parameter of Mg-poor doped and Mg-rich doped samples; and (B) SPB prediction (line) and experimental data (symbols) for the figure of merit versus carrier concentration of Mg-poor and Mg-rich doped samples at 700K. SPB: Single parabolic band.

concentration in the match between theory and model can be expected. Our findings combined with those by Sankhla *et al.*[57] suggest that, although Mg-loss (due to Mg sublimation from an initially Mg-rich composition) can degrade the material properties strongly, combining an initial Mg-deficient compositions with optimized doping can achieve properties similar to those of optimized Mg-rich materials.

CONCLUSIONS

We have demonstrated the successful and reproducible synthesis of single phase Mg-poor n-type $Mg_2(Si,Sn)$ TE materials, and discovered that the material undergoes a self-adjusting synthesis. In fact, it appears that Mg-poor material synthesis is insensitive to the precise nominal composition, which makes the material synthesis suitable for upscaled synthesis. Up to now, Mg-rich compositions were typically employed, first to compensate for Mg loss during synthesis and second to achieve high carrier concentrations. We show here that synthesized Mg-poor samples have highly reproducible and spatially homogeneous thermoelectric properties, presumably due to avoiding loss of excess or loosely bound Mg and second that a sufficiently high carrier concentration can be achieved, despite a reduced dopant efficiency. Moreover, analysis of the transport properties reveals that optimal doping of synthesized Mg-poor solid solutions can achieve transport properties with microscopic parameters comparable to those of synthesized Mg-rich compositions. Furthermore, synthesized Mg-poor samples were compared to samples that were initially synthesized Mg-rich, but experienced Mg-loss, showing that the performances' degradation of the latter was linked to increased grain boundary scattering while in this work we showed that, when the material is synthesized Mg-poor, grain boundary effects are negligible and the material performances are good. Hence, synthesized Mg-rich Mg-depleted and synthesized Mg-poor sample behave differently, leading to very different properties and microscopic parameters. Overall, we show that Mg-poor $Mg_2(Si,Sn)$ materials can exhibit similar or even better TE properties and disprove key arguments for Mg-excess, paving the way for Mg-poor materials, which could exhibit better chemical stability.

DECLARATIONS

Acknowledgements

de Boor, J. would like to acknowledge support and fruitful discussion with Prof. Ernst Bauer during his stay at TU Vienna. The authors also would like to express their gratitude to Przemyslaw Blaschkewitz for his help and assistance with the TE measurements and to Aryan Sankhla for provision of data of Mg-rich samples.

Authors' contributions

Experimentation: Duparchy, A.
Investigation, methodology: Duparchy, A.; de Boor, J.
Materials characterization: Duparchy, A.; Naithani, H: Parzer, M.; Garmroudi, F.; de Boor, J.
Data analysis: Duparchy, A.; Naithani, H: Ghosh, S.; Parzer, M.; Garmroudi, F.; de Boor, J.
Conceptualization and supervision: Müller, E; de Boor, J.
Writing-original draft: Duparchy, A., de Boor, J.
Review and editing: Naithani, H: Ghosh, S.; Parzer, M.; Garmroudi, F.; Müller, E.; de Boor, J.

Availability of data and materials

The original contributions presented in this study are included in the article/Supplementary Materials. Further inquiries can be directed to the corresponding author(s).

Financial support and sponsorship

The authors and the LUNA project team would like to acknowledge the government of North Rhine Westphalia for the funds received to finance the project. The author Duparchy, A. would like to thank the German Academic Exchange Service (DAAD) for the financial support. Financial support for Parzer, M. and Garmroudi, F. came from the Japan Science and Technology Agency (JST), program MIRAI, JPMJMI19A1.

Conflicts of interest

All authors declared that there are no conflicts of interest.

Ethical approval and consent to participate

Not applicable.

Consent for publication

Not applicable.

REFERENCES

1. Gielen, D.; Boshell, F.; Saygin, D. Climate and energy challenges for materials science. *Nat. Mater.* **2016**, *15*, 117-20. DOI PubMed
2. Chu, S.; Majumdar, A. Opportunities and challenges for a sustainable energy future. *Nature* **2012**, *488*, 294-303. DOI PubMed
3. Twaha, S.; Zhu, J.; Yan, Y.; Li, B. A comprehensive review of thermoelectric technology: Materials, applications, modelling and performance improvement. *Renew. Sustain. Energy. Rev.* **2016**, *65*, 698-726. DOI
4. Jaziri, N.; Boughamoura, A.; Müller, J.; Mezghani, B.; Tounsi, F.; Ismail, M. A comprehensive review of thermoelectric generators: technologies and common applications. *Energy. Rep.* **2020**, *6*, 264-87. DOI
5. O'brien, R.; Ambrosi, R.; Bannister, N.; Howe, S.; Atkinson, H. Safe radioisotope thermoelectric generators and heat sources for space applications. *J. Nucl. Mater.* **2008**, *377*, 506-21. DOI
6. Yang, L.; Chen, Z.; Dargusch, M. S.; Zou, J. High performance thermoelectric materials: progress and their applications. *Adv. Energy. Mater.* **2018**, *8*, 1701797. DOI
7. Snyder, G. J.; Toberer, E. S. Complex thermoelectric materials. *Nat. Mater.* **2008**, *7*, 105-14. DOI PubMed
8. Wei, J.; Yang, L.; Ma, Z.; et al. Review of current high-ZT thermoelectric materials. *J. Mater. Sci.* **2020**, *55*, 12642-704. DOI
9. Jia, N.; Cao, J.; Tan, X. Y.; et al. Thermoelectric materials and transport physics. *Mater. Today. Phys.* **2021**, *21*, 100519. DOI
10. Pei, Y.; Shi, X.; LaLonde, A.; Wang, H.; Chen, L.; Snyder, G. J. Convergence of electronic bands for high performance bulk thermoelectrics. *Nature* **2011**, *473*, 66-9. DOI
11. Tang, Y.; Gibbs, Z. M.; Agapito, L. A.; et al. Convergence of multi-valley bands as the electronic origin of high thermoelectric performance in $CoSb_3$ skutterudites. *Nat. Mater.* **2015**, *14*, 1223-8. DOI
12. Yan, X.; Liu, W.; Wang, H.; et al. Stronger phonon scattering by larger differences in atomic mass and size in p-type half-Heuslers $Hf_{1-x}Ti_xCoSb_{0.8}Sn_{0.2}$. *Energy. Environ. Sci.* **2012**, *5*, 7543-8. DOI

13. Liu, Z.; Shuai, J.; Mao, J.; et al. Effects of antimony content in $MgAg_{0.97}Sb_x$ on output power and energy conversion efficiency. *Acta. Mater.* **2016**, *102*, 17-23. DOI
14. Back, S. Y.; Meikle, S.; Mori, T. Comprehensive study of α-MgAgSb: microstructure, carrier transport properties, and thermoelectric performance under ball milling techniques. *J. Mater. Sci. Technol.* **2025**, *227*, 57-66. DOI
15. Imasato, K.; Kang, S. D.; Ohno, S.; Snyder, G. J. Band engineering in Mg_3Sb_2 by alloying with Mg_3Bi_2 for enhanced thermoelectric performance. *Mater. Horiz.* **2018**, *5*, 59-64. DOI
16. Zhang, J.; Song, L.; Sist, M.; Tolborg, K.; Iversen, B. B. Chemical bonding origin of the unexpected isotropic physical properties in thermoelectric Mg_3Sb_2 and related materials. *Nat. Commun.* **2018**, *9*, 4716. DOI
17. Dasgupta, T.; Stiewe, C.; de Boor, J.; Müller, E. Influence of power factor enhancement on the thermoelectric figure of merit in $Mg_2Si_{0.4}Sn_{0.6}$ based materials. *Phys. Status. Solidi. (A).* **2014**, *211*, 1250-4. DOI
18. Liu, W.; Zhang, Q.; Yin, K.; et al. High figure of merit and thermoelectric properties of Bi-doped $Mg_2Si_{0.4}Sn_{0.6}$ solid solutions. *J. Solid. State. Chem.* **2013**, *203*, 333-9. DOI
19. Leblanc, S.; Yee, S. K.; Scullin, M. L.; Dames, C.; Goodson, K. E. Material and manufacturing cost considerations for thermoelectrics. *Renew. Sustain. Energy. Rev.* **2014**, *32*, 313-27. DOI
20. Gaultois, M. W.; Sparks, T. D.; Borg, C. K. H.; Seshadri, R.; Bonificio, W. D.; Clarke, D. R. Data-driven review of thermoelectric materials: performance and resource considerations. *Chem. Mater.* **2013**, *25*, 2911-20. DOI
21. Liu, X.; Zhu, T.; Wang, H.; et al. Low electron scattering potentials in high performance $Mg_2Si_{0.45}Sn_{0.55}$ based thermoelectric solid solutions with band convergence. *Adv. Energy. Mater.* **2013**, *3*, 1238-44. DOI
22. Liu, W.; Tan, X.; Yin, K.; et al. Convergence of conduction bands as a means of enhancing thermoelectric performance of n-type $Mg_2Si_{1-x}Sn_x$ solid solutions. *Phys. Rev. Lett.* **2012**, *108*, 166601. DOI
23. Kaibe, H.; Aoyama, I.; Mukoujima, M.; et al. Development of thermoelectric generating stacked modules aiming for 15% of conversion efficiency. *ICT. 2005. 24th. International. Conference. on. Thermoelectrics,. 2005,.* pp. 242-7. DOI
24. Camut, J.; Müller, E.; de Boor, J. Analyzing the performance of thermoelectric generators with inhomogeneous legs: coupled material-device modelling for Mg_2X-based TEG prototypes. *Energies* **2023**, *16*, 3666. DOI
25. Wieder, A.; Camut, J.; Duparchy, A.; et al. High-performance tellurium-free thermoelectric module for moderate temperatures using α-MgAgSb/Mg_2(Si,Sn). *Mater. Today. Energy.* **2023**, *38*, 101420. DOI
26. Skomedal, G.; Burkov, A.; Samunin, A.; Haugsrud, R.; Middleton, H. High temperature oxidation of Mg_2(Si-Sn). *Corros. Sci.* **2016**, *111*, 325-33. DOI
27. Duparchy, A.; Deshpande, R.; Sankhla, A.; et al. Instability mechanism in thermoelectric Mg_2(Si,Sn) and the role of Mg diffusion at room temperature. *Small. Sci.* **2025**, *5*, 2300298. DOI
28. Kato, D.; Iwasaki, K.; Yoshino, M.; Yamada, T.; Nagasaki, T. Significant effect of Mg-pressure-controlled annealing: non-stoichiometry and thermoelectric properties of $Mg_{2-\delta}Si_{1-x}Sb_x$. *Phys. Chem. Chem. Phys.* **2018**, *20*, 25939-50. DOI PubMed
29. Kato, D.; Iwasaki, K. Mg-pressure-controlled annealing for tuning Mg content and thermoelectric properties of $Mg_{2-\delta}(Si_{0.5}Sn_{0.5})_{1-x}Sb_x$. *J. Alloys. Compd.* **2021**, *856*, 157351. DOI
30. Farahi, N.; Stiewe, C.; Truong, D. Y. N.; de Boor, J.; Müller, E. High efficiency Mg_2(Si,Sn)-based thermoelectric materials: scale-up synthesis, functional homogeneity, and thermal stability. *RSC. Adv.* **2019**, *9*, 23021-8. DOI
31. Sankhla, A.; Patil, A.; Kamila, H.; et al. Mechanical alloying of optimized Mg_2(Si,Sn) solid solutions: understanding phase evolution and tuning synthesis parameters for thermoelectric applications. *ACS. Appl. Energy. Mater.* **2018**, *1*, 531-42. DOI
32. Liu, W.; Tang, X.; Li, H.; Sharp, J.; Zhou, X.; Uher, C. Optimized thermoelectric properties of Sb-doped $Mg_{2(1+Z)}Si_{0.5-y}Sn_{0.5}Sb_y$ through adjustment of the Mg content. *Chem. Mater.* **2011**, *23*, 5256-63. DOI
33. Macario, L. R.; Cheng, X.; Ramirez, D.; Mori, T.; Kleinke, H. Thermoelectric properties of Bi-doped magnesium silicide stannides. *ACS. Appl. Mater. Interfaces.* **2018**, *10*, 40585-91. DOI PubMed
34. Sankhla, A.; Kamila, H.; Naithani, H.; Mueller, E.; de Boor, J. On the role of Mg content in Mg_2(Si,Sn): assessing its impact on electronic transport and estimating the phase width by in situ characterization and modelling. *Mater. Today. Phys.* **2021**, *21*, 100471. DOI
35. Ghosh, S.; Abdelbaky, M.; Mertin, W.; Müller, E.; de Boor, J. Surface degradation of Mg_2X-based composites at room temperature: assessing grain boundary and bulk diffusion using atomic force microscopy and scanning electron microscopy. *ACS. Appl. Mater. Interfaces.* **2024**, *16*, 48619-28. DOI PubMed PMC
36. Sankhla, A. Unraveling the interplay between composition, electronic band structure and electronic transport properties in n-type Mg_2X (X: Si, Sn) materials. Ph.D. Dissertation, Justus Liebig University Giessen, Giessen, 2024. https://jlupub.ub.uni-giessen.de/items/f291cf47-c09c-4c5d-b7c3-864e7a58abd0 (accessed 2025-06-05).
37. Liu, Z.; Geng, H.; Mao, J.; et al. Understanding and manipulating the intrinsic point defect in α-MgAgSb for higher thermoelectric performance. *J. Mater. Chem. A.* **2016**, *4*, 16834-40. DOI
38. Ryu, B.; Choi, E.; Park, S.; et al. Native point defects and low p-doping efficiency in Mg_2(Si,Sn) solid solutions: a hybrid-density functional study. *J. Alloys. Compd.* **2021**, *853*, 157145. DOI
39. Wood, M.; Kuo, J. J.; Imasato, K.; Snyder, G. J. Improvement of low-temperature *zT* in a Mg_3Sb_2-Mg_3Bi_2 solid solution via Mg-vapor annealing. *Adv. Mater.* **2019**, *31*, e1902337. DOI
40. Imasato, K.; Wood, M.; Anand, S.; Kuo, J. J.; Snyder, G. J. Understanding the high thermoelectric performance of Mg_3Sb_2-Mg_3Bi_2 alloys. *Adv. Energy. Sustain. Res.* **2022**, *3*, 2100208. DOI

41. Ohno, S.; Imasato, K.; Anand, S.; et al. Phase boundary mapping to obtain n-type Mg_3Sb_2-based thermoelectrics. *Joule* **2018**, *2*, 141-54. DOI
42. Adekoya, A. H.; Snyder, G. J. Thermodynamic modeling of Bi_2Te_3 in the defect energy formalism. *Mater. Today. Electron.* **2024**, *9*, 100109. DOI
43. Liu, Z.; Sato, N.; Gao, W.; et al. Demonstration of ultrahigh thermoelectric efficiency of ~7.3% in Mg_3Sb_2/MgAgSb module for low-temperature energy harvesting. *Joule* **2021**, *5*, 1196-208. DOI
44. Ying, P.; Villoro, R. B.; Bahrami, A.; et al. Performance degradation and protective effects of atomic layer deposition for Mg-based thermoelectric modules. *Adv. Funct. Mater.* **2024**, *34*, 2406473. DOI
45. Kamila, H.; Ryu, B.; Ayachi, S.; Sankhla, A.; Mueller, E.; de Boor, J. Understanding the dopability of p-type $Mg_2(Si,Sn)$ by relating hybrid-density functional calculation results to experimental data. *J. Phys. Energy.* **2022**, *4*, 035001. DOI
46. Kamila, H.; Sankhla, A.; Yasseri, M.; et al. Synthesis of p-type $Mg_2Si_{1-x}Sn_x$ with x = 0-1 and optimization of the synthesis parameters. *Mater. Today. Proc.* **2019**, *8*, 546-55. DOI
47. Nolas, G. S.; Wang, D.; Beekman, M. Transport properties of polycrystalline $Mg2Si_{1-y}Sb_y$ ($0 \leq y < 0.4$). *Phys. Rev. B.* **2007**, *76*, 235204. DOI
48. Dasgupta, T.; Stiewe, C.; Hassdorf, R.; Zhou, A. J.; Boettcher, L.; Mueller, E. Effect of vacancies on the thermoelectric properties of $Mg_2Si_{1-x}Sb_x$ ($0 \leq x \leq 0.1$). *Phys. Rev. B.* **2011**, *83*, 235207. DOI
49. Hwang, J. D.; Wang, W. J. Application of ICP-AES to analysis of solutions. *Appl. Spectrosc. Rev.* **1995**, *30*, 231-350. DOI
50. Potts, P. J. Inductively coupled plasma-atomic emission spectrometry. In *A handbook of a handbook of silicate rock analysis*, 1th ed.; Springer Book Archive, Springer, 1987;pp 153-97. DOI
51. Zachariadis, G. *Inductively coupled plasma atomic emission spectrometry : a model multi-elemental technique for modern analytical laboratory*; Nova Science Publishers, 2012. https://ikee.lib.auth.gr/record/271630 (accessed 2025-06-05).
52. Ziolkowski, P.; Karpinski, G.; Platzek, D.; Stiewe, C.; Muller, E. Application overview of the potential seebeck microscope. In *2006 25th International Conference on Thermoelectrics*, Vienna, Austria, IEEE, 2006; pp 684-8. DOI
53. Platzek, D.; Karpinski, G.; Stiewe, C.; Ziolkowski, P.; Drasar, C.; Muller, E. Potential-Seebeck-microprobe (PSM): measuring the spatial resolution of the Seebeck coefficient and the electric potential. In *ICT 2005. 24th International Conference on Thermoelectrics, 2005*, Clemson, SC, USA, IEEE, 2005; pp 13-6. DOI
54. de Boor, J.; Stiewe, C.; Ziolkowski, P.; et al. High-Temperature measurement of seebeck coefficient and electrical conductivity. *J. Electron. Mater.* **2013**, *42*, 1711-8. DOI
55. Boor J, Müller E. Data analysis for seebeck coefficient measurements. *Rev. Sci. Instrum.* **2013**, *84*, 065102. DOI PubMed
56. Parzer, M. Extending the phase space of thermoelectric full-Heusler compounds. Ph.D. Dissertation, Technische Universität Wien, 2024. DOI
57. Sankhla, A.; Kamila, H.; Kelm, K.; Mueller, E.; de Boor, J. Analyzing thermoelectric transport in n-type $Mg_2Si_{0.4}Sn_{0.6}$ and correlation with microstructural effects: an insight on the role of Mg. *Acta. Mater.* **2020**, *199*, 85-95. DOI
58. Snyder, G. J.; Snyder, A. H.; Wood, M.; Gurunathan, R.; Snyder, B. H.; Niu, C. Weighted mobility. *Adv. Mater.* **2020**, *32*, e2001537. DOI PubMed
59. Naithani, H.; Müller, E.; de Boor, J. Uncertainty analysis of microscopic parameters obtained from the single parabolic band (SPB) modelling of thermoelectrics materials. In *Proceedings of the 41st International and 7th Asian Conference on Thermoelectrics (ICT/ACT 2025)*, Sendai, Japan, 2025; Paper 16-A-O-023. https://ict2025.jp/item/ICT2025_Oral_abstract_protected.pdf (accessed 2025-07-09).
60. Castillo-hernandez, G.; Yasseri, M.; Klobes, B.; Ayachi, S.; Müller, E.; de Boor, J. Room and high temperature mechanical properties of Mg_2Si, Mg_2Sn and their solid solutions. *J. Alloys. Compd.* **2020**, *845*, 156205. DOI
61. Assahsahi, I.; Popescu, B.; El, B. R.; Zejli, D.; Enculescu, M.; Galatanu, A. Thermoelectric properties of p-type $Mg_2Si_{0.3}Sn_{0.7}$ doped with silver and gallium. *J. Alloys. Compd.* **2023**, *944*, 169270. DOI
62. Yasseri, M.; Sankhla, A.; Kamila, H.; et al. Solid solution formation in $Mg_2(Si,Sn)$ and shape of the miscibility gap. *Acta. Mater.* **2020**, *185*, 80-8. DOI
63. Yasseri, M.; Mitra, K.; Sankhla, A.; de Boor, J.; Müller, E. Influence of Mg loss on the phase stability in Mg_2X (X=Si, Sn) and its correlation with coherency strain. *Acta. Mater.* **2021**, *208*, 116737. DOI
64. Ai, X.; Xue, W.; Giebeler, L.; et al. Interstitial defect modulation promotes thermoelectric properties of *p*-Type HfNiSn. *Adv. Energy. Mater.* **2024**, *14*, 2401345. DOI
65. He, S.; Bahrami, A.; Ying, P.; et al. Improving the thermoelectric performance of ZrNi(In,Sb)-based double half-Heusler compounds. *J. Mater. Chem. A.* **2022**, *10*, 13476-83. DOI
66. Edler, F.; Huang, K. Analysis of the "cold finger effect" in measuring the Seebeck coefficient. *Meas. Sci. Technol.* **2020**, *32*, 035014. DOI
67. Kato, D.; Iwasaki, K.; Yoshino, M.; Yamada, T.; Nagasaki, T. Control of Mg content and carrier concentration via post annealing under different Mg partial pressures for Sb-doped Mg_2Si thermoelectric material. *J. Solid. State. Chem.* **2018**, *258*, 93-8. DOI
68. Zhang, L.; Chen, X.; Tang, Y.; et al. Thermal stability of $Mg_2Si_{0.4}Sn_{0.6}$ in inert gases and atomic-layer-deposited Al_2O_3 thin film as a protective coating. *J. Mater. Chem. A.* **2016**, *4*, 17726-31. DOI
69. Nieroda, P.; Mars, K.; Nieroda, J.; et al. New high temperature amorphous protective coatings for Mg_2Si thermoelectric material. *Ceram. Int.* **2019**, *45*, 10230-5. DOI

70. Yin, K.; Zhang, Q.; Zheng, Y.; Su, X.; Tang, X.; Uher, C. Thermal stability of $Mg_2Si_{0.3}Sn_{0.7}$ under different heat treatment conditions. *J. Mater. Chem. C.* **2015**, *3*, 10381-7. DOI
71. Deshpande, R.; Bahrami, A.; Kreps, F.; et al. On the origin of temperature induced performance degradation of Cu-contacted Mg_2X-based (X = Si, Sn) thermoelectric materials. *ACS. Appl. Mater. Interfaces.* **2025**, *17*, 28777-88. DOI
72. Deshpande, R.; Bahrami, A.; Kreps, F.; et al. On the origin of temperature induced performance degradation of Cu-contacted Mg_2X-based (X=Si, Sn) thermoelectric materials. *ACS. Appl. Mater. Interfaces.* **2025**, *17*, 28777-88. DOI
73. Orenstein, R.; Male, J. P.; Toriyama, M.; Anand, S.; Snyder, G. J. Using phase boundary mapping to resolve discrepancies in the Mg_2 Si-Mg_2Sn miscibility gap. *J. Mater. Chem. A.* **2021**, *9*, 7208-15. DOI
74. Yi, S.; Attari, V.; Jeong, M.; et al. Strain-induced suppression of the miscibility gap in nanostructured Mg_2Si-Mg_2Sn solid solutions. *J. Mater. Chem. A.* **2018**, *6*, 17559-70. DOI
75. Ayachi, S.; Deshpande, R.; Ponnusamy, P.; et al. On the relevance of point defects for the selection of contacting electrodes: Ag as an example for Mg_2(Si,Sn)-based thermoelectric generators. *Mater. Today. Phys.* **2021**, *16*, 100309. DOI
76. Liu, W.; Chi, H.; Sun, H.; et al. Advanced thermoelectrics governed by a single parabolic band: $Mg_2Si_{0.3}Sn_{0.7}$, a canonical example. *Phys. Chem. Chem. Phys.* **2014**, *16*, 6893-7. DOI
77. May, A. F.; Snyder, G. J. *Materials, preparation, and characterization in thermoelectrics*; Rowe DM, Ed.; CRC Press: 2012. DOI
78. Harrison, J. W.; Hauser, J. R. Alloy scattering in ternary III-V compounds. *Phys. Rev. B.* **1976**, *13*, 5347-50. DOI
79. Wang, H.; Lalonde, A. D.; Pei, Y.; Snyder, G. J. The criteria for beneficial disorder in thermoelectric solid solutions. *Adv. Funct. Mater.* **2013**, *23*, 1586-96. DOI
80. Bardeen, J.; Shockley, W. Deformation potentials and mobilities in non-polar crystals. *Phys. Rev.* **1950**, *80*, 72-80. DOI
81. de Boor, J.; Dasgupta, T.; Kolb, H.; Compere, C.; Kelm, K.; Mueller, E. Microstructural effects on thermoelectric efficiency: a case study on magnesium silicide. *Acta. Mater.* **2014**, *77*, 68-75. DOI
82. Kuo, J. J.; Kang, S. D.; Imasato, K.; et al. Grain boundary dominated charge transport in Mg_3Sb_2-based compounds. *Energy. Environ. Sci.* **2018**, *11*, 429-34. DOI
83. Kuo, J. J.; Yu, Y.; Kang, S. D.; Cojocaru-mirédin, O.; Wuttig, M.; Snyder, G. J. Mg deficiency in grain boundaries of n-type Mg_3Sb_2 identified by atom probe tomography. *Adv. Mater. Interfaces.* **2019**, *6*, 1900429. DOI
84. Seto, J. Y. W. The electrical properties of polycrystalline silicon films. *J. Appl. Phys.* **1975**, *46*, 5247-54. DOI
85. Agrawal, B.; de Boor, J.; Dasgupta, T. A multi-band refinement technique for analyzing electronic band structure of thermoelectric materials. *Cell. Rep. Phys. Sci.* **2024**, *5*, 101781. DOI
86. de Boor, J.; Compere, C.; Dasgupta, T.; et al. Fabrication parameters for optimized thermoelectric Mg_2Si. *J. Mater. Sci.* **2014**, *49*, 3196-204. DOI
87. Fistul', V. I. Transport phenomena in heavily doped semiconductors, In *Heavily doped semiconductors*, vol 1; Springer, Boston, MA, 1969;pp 77-205 DOI